

Homogenized Strain Model for Ni–Mn–Ga Driven with Collinear Magnetic Field and Stress

LEANN E. FAIDLEY, MARCELO J. DAPINO* AND GREGORY N. WASHINGTON

*Department of Mechanical Engineering, The Ohio State University
201 West 19th Avenue, Columbus, OH 43210, USA*

ABSTRACT: Prior experimental measurements by the authors demonstrated large reversible strains of -0.41% along the $[001]$ crystal direction of a cylindrical $\text{Ni}_{50}\text{Mn}_{28.7}\text{Ga}_{21.3}$ rod driven with a magnetic field along the same direction and no external restoring force. The origin of the reversibility is attributed to internal bias stresses generated by impurities absorbed during manufacture of the alloy. This article presents a macroscopic constitutive model for Ni–Mn–Ga strain in collinear field and stress configuration. The switching between two variant orientations in the presence of Zeeman energy and the pinning energy of the impurities is formulated through a Gibbs energy function for the crystal lattice. Inhomogeneous local interaction fields and impurity distributions are addressed through stochastic homogenization techniques. Attributes of the model are illustrated through comparison of model results with strain–field measurements collected at various compressive loads. Constrained optimization is used to determine the necessary parameters and an error analysis is performed to assess the accuracy of the model for various loading conditions. The collinear field and stress configuration can lead to solenoid transducers with enhanced energy density and bandwidth relative to standard electromagnet devices.

Key Words: Ferromagnetic shape memory, Ni–Mn–Ga, free energy modeling, multi-scale homogenization, actuation.

INTRODUCTION

LARGE magnetic field-induced strains (MFISs) as large as 9.5% have been observed in nickel manganese gallium (Ni–Mn–Ga) martensites exposed to magnetic fields of 400 kA/m (Likhachev et al., 2001; Murray et al., 2001; Sozinov et al., 2002). Due to the field activation, the frequency response of Ni–Mn–Ga alloys can be higher than that exhibited through thermal activation in shape memory alloys (Faidley et al., 2003). These properties are significant for actuator and sensor applications in emerging technological areas in which increasing performance demands dictate the need for transducer materials capable of large deformations simultaneously with broad frequency bandwidths.

As is the case with shape memory materials, the large deformations exhibited by Ni–Mn–Ga alloys originate in the rearrangement of martensitic twin variants under the action of magnetic fields. Unlike nickel titanium and other shape memory materials, in which the ability to do work stems from thermomechanical transformation between the martensite and austenite phases, the main

actuation mechanism in Ni–Mn–Ga takes place in the low-temperature martensite phase and is driven by magnetic fields or mechanical stresses. Since in Ni–Mn–Ga magnetic fields and compressive stresses applied collinearly favor the same variant, a mechanical force or magnetic field must be applied orthogonal to the driving magnetic field to restore the twin variants and thus obtain bidirectional deformations. In applications, this is done by placing a rectangular sample in an electromagnet with the magnetic field applied along the $[110]$ crystallographic direction of the parent phase and a bias compressive stress applied along the $[001]$ direction (Tickle, 2000).

Models for twin variant rearrangement in ferromagnetic shape memory alloys have been constructed both from microscopic principles (James and Wuttig, 1998; DeSimone and James, 2006) and macroscopic thermodynamic considerations (O’Handley, 1998; Murray et al., 2000). The former approach tends to be more general and accurate but at the expense of computational efficiency, hence its implementation often is restricted to highly simplified cases. Thermodynamic formulations often include the difference in Zeeman energy across the twin boundaries as the driving force for twin rearrangement, on the assumption that the

*Author to whom correspondence should be addressed.

E-mail: dapino.1@osu.edu

Figures 1, 8, 9 and 11–15 appear in color online: <http://jim.sagepub.com>

anisotropy energy is much larger than the Zeeman energy. For those situations in which the anisotropy energy is small, drive magnetic fields align the magnetization vectors without rotating the unit cells, thus leading to a small MFIS. For intermediate anisotropy energies, both effects take place leading to saturation behavior in the strain-field curves. After formulating the total energy as a combination of appropriate driving energies and the elastic energy, minimization with respect to volume fraction leads to constitutive expressions for strain and magnetization.

Prior literature on parallel field and stress configurations is virtually nonexistent. Wu et al. (1999) have reported a large recoverable MFIS of -0.31% in the $[001]$ direction of an off-stoichiometry single crystal of $\text{Ni}_{52}\text{Mn}_{22.2}\text{Ga}_{25.8}$ driven by a 20 kOe field along the $[001]$ direction. This alloy showed a martensitic self-strain of 2%, about a hundred times as large as that of Ni_2MnGa , thus suggesting that the martensite variants in a large fraction of the alloy are preferentially oriented. This reduces the degree of self-accommodation and leads to reduced deformations compared with the 6% strains achievable by reorientation of the c -axis throughout the alloy. The measured deformations are very significant, nonetheless, as they compare favorably with those of Terfenol-D. However, the combination of high fields and low martensitic transformation temperature, which in this alloy is situated slightly below room temperature, precludes the practical implementation of this alloy in motion generation systems. Ohmic and eddy current heating produced within the solenoid transducer would easily cause the alloy to transform to its austenitic phase.

Malla et al. (2006) have established that large reversible strains of -0.41% are possible in $\text{Ni}_{50}\text{Mn}_{28.7}\text{Ga}_{21.3}$ exposed to alternating magnetic fields along the $[001]$ direction of the parent austenite phase with *no external restoring force*. This unexpected result suggests the presence of internal bias stresses in the alloy which act as localized energy potentials that oppose twin boundary motion and provide an otherwise nonexistent restoring force when the magnetic field is removed. The presence of internal restraining forces also explains the reduced deformations relative to alloys capable of over 6% strain, in which twin boundary motion is largely unimpeded. The bidirectional deformations and associated macroscopic magneto-mechanical behaviors (Malla et al., 2006) have remained unaltered after the alloy, which was tested as cast without mechanical 'training', was subjected to a large number of field and stress cycles (Malla et al., 2006). While this effect could stem from a number of mechanisms at the lattice level, impurities are the most likely cause of stable internal stresses in the alloy. It has been shown that Ni-Mn-Ga alloys are extremely susceptible to impurities; inclusions of

gallium sulfide (S), tantalum (Ta) plates of various shapes and sizes, and titanium-rich (Ti) precipitates have been observed (Richard, 2005). It was assumed that for the large, incoherent S and Ta inclusions observed, twin boundaries would have to loop around the impurities in order for twin boundary motion to occur. Since the observed Ti precipitates are much smaller than the S and Ta inclusions, it was argued that the mechanism of twin boundary motion in the presence of Ti precipitates is most likely cutting through the particles, as opposed to looping. By cutting, the twin boundaries form two new interfaces which provide a low-energy path for twin boundary movement as compared to looping around the particles. It was estimated that the small Ti-rich precipitates have a strength of $\sim 0.53 K_u$, with K_u the uniaxial anisotropy constant; thus they could be overcome by the application of sufficiently large magnetic fields. These small precipitates do not seem to impact the MFIS of the alloys studied as strains of 6% were observed.

This article is focused on the development and implementation of a macroscopic constitutive model for twin boundary rearrangement in the presence of impurities and associated pinning energies. As hypothesized by Malla et al. (2006), low-energy impurities do not contribute to the mechanism for reversible MFIS in the alloy investigated; during the first few field cycles after manufacture of the alloy, the twin boundaries have unattached from these sites and permanently attached to higher energy sites. Hence, the model is constructed on the assumption that twin boundaries are normally pinned to impurities whose energy is greater than the anisotropy energy. The model provides an additional component to the current description of the strain mechanism in Ni-Mn-Ga and lays the groundwork for future work on implementation and control of solenoid Ni-Mn-Ga transducers like that shown in Figure 1. Because solenoid transducers can be

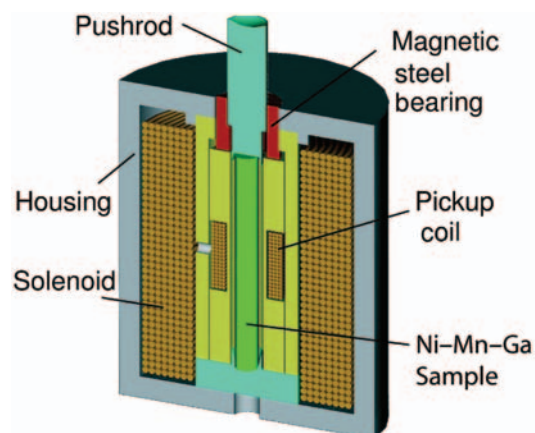


Figure 1. Solenoid Ni-Mn-Ga transducer for use in dynamic actuator and sensor applications.

designed around a closed magnetic circuit, they can potentially offer higher efficiency and enhanced frequency bandwidth relative to their electromagnet counterparts. These enhanced properties can possibly offset the reduced deformations produced by the Ni–Mn–Ga element in this configuration.

The article starts with a discussion of the strain mechanism in Ni–Mn–Ga for materials without and with twin boundary impediment by impurities. The constitutive model, which is presented thereafter, comprises two main components. The first component employs a Gibbs energy function to quantify twin boundary motion in the presence of an orthogonal pair formed by a uniaxial magnetic field and internal bias stresses associated with impurities in the alloy. The model is formulated by considering the Zeeman, elastic, and pinning energies. This component of the model is an extension of a phenomenological model presented by Kiefer and Lagoudas (2004). The resulting constitutive relations quantify the local average strain for single crystal materials and does not account for the variability in the density and strength of the impurities throughout the material. This variability is addressed in this article by considering stochastic homogenization techniques that are constructed on the assumption that local coercive fields and pinning energies are manifestations of underlying distributions. This approach has been developed by Smith et al. for ferroelectric materials, ferromagnetic materials, and shape memory alloys (Smith et al., 2003, 2006; Smith, 2005; Smith and Dapino, 2005). Model parameters were obtained through constrained optimization from experimental data under several loading conditions. A comparison between model results and measurements is presented by means of an error analysis for the various sets of identified parameters.

STRAIN MECHANISMS

The strain mechanism for Ni–Mn–Ga is well established (Tickle and James, 1999; Likhachev and Ullakko, 2000). As Ni–Mn–Ga cools from the high-temperature austenite phase to the low-temperature martensite phase, a self-accommodating twinned structure results due to the minimization of the strain energy generated from the mismatch between the cubic and tetragonal lattices. A simplified 2D representation of this twinned structure is shown in Figure 2. At zero field, the material consists of two perpendicular variants which are separated by a twin boundary as illustrated in panel (a). Each variant consists of several distinct magnetic domains which are divided by 180° walls. The magnetic domain volume fraction is denoted by a . At small transverse fields H , all of the magnetization vectors remain aligned with the magnetically easy, short

c -axis of each variant and the magnetic domains disappear as shown in panel (b). Since we are interested in the behaviors at medium to large fields, $a = 1$ is assumed.

As a transverse field is applied, the variants favored by the field will increase in size through twin variant rearrangement. Alloys in the Ni–Mn–Ga system have large magnetic anisotropy energies compared to the energy necessary to reorient the unit cells at the twin boundary. Thus, as the magnetization vectors attempt to align with the applied magnetic field, the unit cells along the twin boundary will switch orientation such that their c -axis is more closely aligned with the field. This results in the growth of favorable variants at the expense of unfavorable ones through twin boundary motion and the overall axial lengthening of the bulk sample, as depicted in panel (c). As the field is increased to the point where no further twin boundary motion is possible and the field energy overcomes the magnetic anisotropy energy, the local magnetization vectors break away from the c -axis and align with the field. This results in magnetic saturation as shown in panel (d). When the field is removed, as in panel (e), the magnetic anisotropy energy will restore the local magnetization to the c -axis of the unit cells. Since both variants are equally favorable from an energy standpoint, (Murray et al., 2000) there is no restoring force to cause the reorientation of the unit cell and the size of the

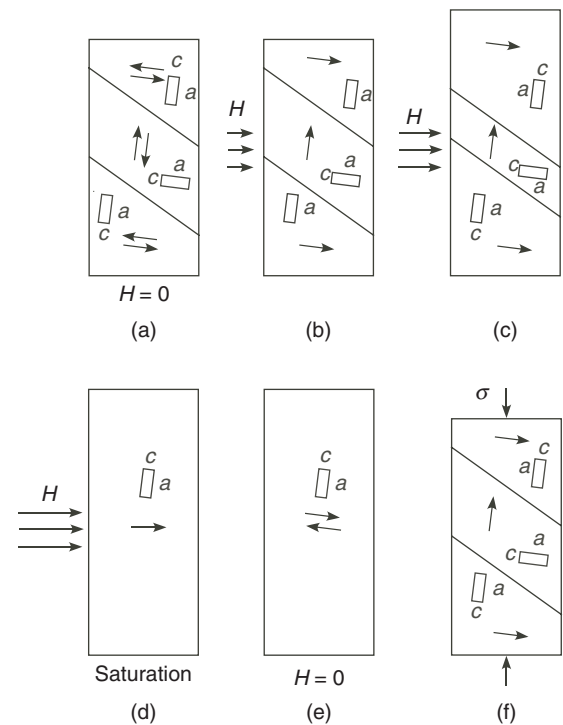


Figure 2. Bidirectional strain mechanism for Ni–Mn–Ga under an orthogonal field–stress pair: (a) no field applied; (b)–(d) sample elongation due to increasing field; (e) sample length remains unchanged when field is removed; and (f) sample contraction due to a compressive stress.

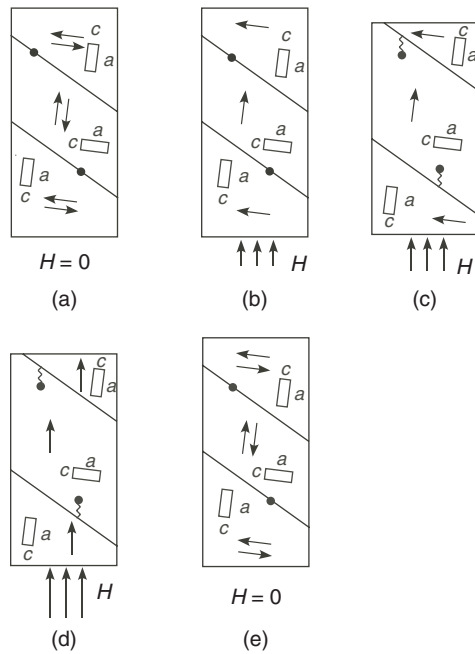


Figure 3. Strain mechanism for Ni–Mn–Ga driven by a collinear stress and field pair in the presence of impurities: (a) no field applied; (b)–(d) sample contraction due to increasing field; and (e) return to original length when the field is removed.

sample will not change upon removal of the field. Twin boundary motion and reversible strain can be induced by applying an axial field, axial compressive stress, or a transverse tensile stress, all of which favor the variant with the short c aligned with the axial direction; see panel (f).

We propose a modification to the mechanism described in Figure 2 to include the effect of impurities in the martensite. The twin boundaries are normally pinned to the impurities – represented by black dots in Figure 3 – which have energies larger in magnitude than the anisotropy energy of the sample. The impurities have been shown to have varying pinning energies (Marioni et al., 2004).

When exposed to axial magnetic fields, the twin boundaries attempt to displace according to the standard mechanisms for twin variant rearrangement, as in panels (b)–(c), but the field does not provide enough energy to overcome the energy barrier provided by the impurities. Instead, the twin boundaries loop around the impurities and as they do work against the pinning energy, energy is dissipated. Saturation is achieved when the field energy is large enough to overcome the anisotropy energy and the magnetic moments align with the field without changing the orientation of the crystal, as shown in panel (d). When the field is removed (panel (e)) the anisotropy energy returns the magnetic moments to the easy c -axis of the crystal and the pinning energy provides a restoring mechanism for the twin boundary, returning the sample

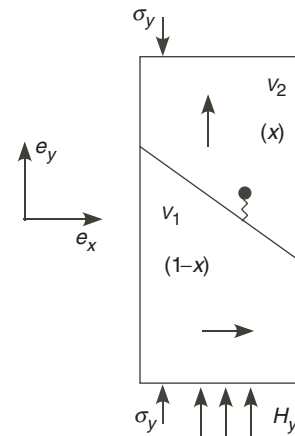


Figure 4. Two-dimensional variants: notation and orientation.

to its original length and magnetization. This theory provides an explanation for the smaller magnitude of strain possible from the alloy investigated and for the reversibility of the strain when the magnetic field is cycled.

MODEL

The strain produced by Ni–Mn–Ga driven by collinear magnetic fields and stresses is quantified in two steps. In the first, a thermodynamic approach is formulated which builds on a previous model for FSMA's proposed by Kiefer and Lagoudas (2004) for conventional perpendicular magnetic fields and stresses. An additional term due to internal orthogonal stresses which quantifies the restoring force found in our experiments is included in the Gibbs energy function (Faidley et al., 2005). The model quantifies the strain generated by single crystalline two-variant systems in which the pinning density and magnetic field are homogeneous throughout. Under these conditions the model yields ‘blocky’ strain–field curves which are not consistent with the mollified responses exhibited by real engineered materials. In the second step of model development, this shortcoming is addressed by considering a homogenization procedure (Smith, 2005) whereby the pinning strength and local magnetic fields are assumed to be stochastically distributed rather than constant. This yields a formulation which characterizes the evolution of volume fractions in Ni–Mn–Ga alloys driven by collinear magnetic fields and stresses in the presence of internal restoring forces.

Free Energy Formulation

For simplicity, we assume that the structure comprises two variant orientations described by the 2D representation shown in Figure 4. Variant 2 is that

which is favored by an axially applied field in the longitudinal direction and has a volume fraction of x . Variant 1 is the transverse variant with magnetization vectors oriented orthogonal to the applied field and a volume fraction of $(1 - x)$.

The material described in Figure 4 can thus be treated as a mixture of variants. The specific energy for this system is given by

$$G(\boldsymbol{\sigma}, \mathbf{H}, T) = (1 - x)G^{v_1} + xG^{v_2} + G^b \quad (1)$$

where G^{vi} is the energy of the i -th variant and G^b is the energy of the boundary between the two variants. It is assumed that the system is isothermal and the fields are large enough to ensure that the effects of the magnetic domains can be ignored. In this case, the expression for the energy of each variant simplifies to the standard expression for specific Gibbs free energy (Bozorth, 1951; Smith, 2005)

$$G^{vi}(\boldsymbol{\sigma}, \mathbf{H}, T = \text{const}) = \psi^{vi} - \frac{1}{2\rho} \boldsymbol{\sigma} \cdot \mathbf{S}^{vi} \boldsymbol{\sigma} - \frac{\mu_0}{\rho} \mathbf{M}^{vi} \cdot \mathbf{H} \quad (2)$$

where for the i -th variant, ψ^{vi} is the Helmholtz energy, $\boldsymbol{\sigma}$ is the applied stress, \mathbf{S}^{vi} is the mechanical compliance, \mathbf{M}^{vi} is the magnetization, \mathbf{H} is the applied field, ρ is the density, and μ_0 is the permeability of free space.

The energy of the twin boundary stems from two sources. The first is the energy necessary to rotate a unit cell, which can be expressed as work done to overcome a force. The second is the energy of the impurities, which can be modeled as that of a mechanical spring. Thus the boundary energy term has the form

$$G^b = \begin{cases} c_1x + k_1x^2 & \dot{x} > 0 \\ c_2x + k_2x^2 & \dot{x} < 0 \end{cases} \quad (3)$$

where k is the effective spring constant of the impurities, c is the energy associated with cell rearrangement and the two branches of the function occur because the behavior of the material is not the same when the field is increasing and variant 1 is growing as it is when the field is decreasing and variant 1 is shrinking. It is noted that this expression has the same form as the hardening function employed by Keifer and Lagoudas (2004) on the basis of shape memory arguments.

For the solenoid transducer shown in Figure 1, both the applied stress and applied field are in the axial direction. Using the geometry specified in Figure 4, substitution of (2) and (3) into (1) yields

$$\begin{aligned} G(\boldsymbol{\sigma}, \mathbf{H}, T = \text{const}) = & \psi^{v_1} - \frac{1}{2\rho} S_{yy}^{v_1} \sigma_y^2 \\ & + x \left[-\frac{1}{2\rho} \Delta S_{yy} \sigma_y^2 - \frac{\mu_0 M_s}{\rho} H_y \right] \\ & + \begin{cases} c_1x + k_1x^2 & \dot{x} > 0 \\ c_2x + k_2x^2 & \dot{x} < 0 \end{cases} \end{aligned} \quad (4)$$

where the Δ operator refers to the difference between the two variants and $\Delta\psi = 0$ since the Helmholtz energies of the two variants are identical. Having now derived an expression for the free energy, expressions for various thermodynamic quantities can be developed. The particular relation of interest comes about through the Clausius–Duhem version of the second law of thermodynamics, which states that for a reversible process

$$\pi^x = \epsilon_s \sigma_y - \rho \frac{\partial G}{\partial x} \quad (5)$$

where $\pi^x = \pm Y^x$ is the condition for the onset of twin variant motion and ϵ_s is the saturation strain. Differentiation of (4) and substitution into (5) yields the force balance

$$\pm Y^x = \epsilon_s \sigma_y - \frac{1}{2} \Delta S_{yy} \sigma_y^2 - \mu_0 M_s H_y - \rho \begin{cases} c_1 + 2k_1x \\ c_2 + 2k_2x \end{cases} \quad (6)$$

for the respective cases $\{\dot{x} > 0\}$ and $\{\dot{x} < 0\}$. Expression (6) can then be solved for the volume fraction,

$$x = \begin{cases} A_1(\epsilon_s \sigma_y + \frac{1}{2} \Delta S_{yy} \sigma_y^2 + \mu_0 M_s H_y - \rho c_1 - Y^x) & \dot{x} > 0 \\ A_2(\epsilon_s \sigma_y + \frac{1}{2} \Delta S_{yy} \sigma_y^2 + \mu_0 M_s H_y - \rho c_2 + Y^x) & \dot{x} < 0 \end{cases} \quad (7)$$

which is dependent on the applied field H_y and axial stress σ_y . Here, $A_1 = 1/(2\rho k_1)$ and $A_2 = 1/(2\rho k_2)$. To facilitate the implementation, expression (7) is rewritten as

$$x = \begin{cases} A_1(\epsilon_s \sigma_y + \frac{1}{2} \Delta S_{yy} \sigma_y^2 + \mu_0 M_s H_y - \rho c_1 - Y^x) \\ x_s \\ A_2(\epsilon_s \sigma_y + \frac{1}{2} \Delta S_{yy} \sigma_y^2 + \mu_0 M_s H_y - \rho c_2 + Y^x) \end{cases} \quad (8)$$

for the respective cases $\{\dot{H} > 0 \text{ and } x < x_s\}$, $\{x > x_s\}$ and $\{\dot{H} < 0 \text{ and } x < x_s\}$. The strain is related to the volume fraction by

$$\epsilon = x\epsilon_{th}, \quad (9)$$

with ϵ_{th} the maximum theoretical strain which would occur if a single boundary swept through the entire material, thus producing a change in x from 0 to 1. Hence, for the case where the twin boundaries are restrained by impurities, x will be limited to a much smaller range. Parameters that need to be identified in this model include k_1 , k_2 , ϵ_s , ΔS_{yy} , M_s , c_1 , c_2 , and Y^x .

Stochastic Homogenization

Relation (8) provides a model for the strain generated by single crystal Ni–Mn–Ga with its twin boundaries

partially restrained by impurities, exposed to collinear magnetic fields and external stresses. The limitations of the model and a sensitivity analysis relating model accuracy with parameter selection were discussed by Faidley et al. (2005). The most critical sources of error in this model include:

- (i) The sample is assumed to consist of only two variants with a single boundary. In reality, however, Ni–Mn–Ga has many twin variants though only two distinct orientations. This implies that a sample will have numerous twin boundaries and a potentially large number of impurities to which the boundaries can attach.
- (ii) The impurities are assumed to be homogeneously distributed throughout the material and each impurity has the same energy. As discussed by Marioni et al. (2004), in a physical material the pinning energies vary over a large range which translates into a variation of the slopes k_1 and k_2 . The energy of each site depends on how it interacts with the surrounding microstructure. Furthermore, the strength of each site may depend on the direction of motion of the twin boundary, effectively providing a source of anisotropy.
- (iii) The field is assumed to be uniform throughout the sample. However, due to short-range interactions, the magnetic field in Ni–Mn–Ga can be considered to behave locally in a fashion similar to the Weiss mean field (Jiles, 1995). Thus, the magnitude of the field at a given point in the material is not equal to the applied field but rather, is given by an effective field which is dependent on the applied field and the magnetization, $H_e = H + H_i = H + \alpha M$. The mean field constant α varies from point to point in the material due to differences in the lattice structure.

Limiting factors (i)–(iii) are addressed in this article by considering stochastic homogenization in the sense of Smith (2005). This approach has proven effective for modeling polarization hysteresis in the presence of thermal activation and stresses in ferroelectric materials, ferromagnetic materials, and shape memory alloys. Special features of the model include its ability to address reversible and irreversible behaviors, biased and unbiased minor loop regimes including accommodation effects, and relaxation phenomena (Smith and Dapino, 2005; Smith et al., 2006). The effects of polycrystallinity, material nonhomogeneities, inclusions, textures, and variable interaction fields are incorporated in the Smith model for ferromagnetic materials by assuming that the local coercive field H_c and interaction field H_i are stochastically distributed with respective densities v_1 and v_2 , which are chosen to satisfy specific

decay criteria. The resulting macroscopic magnetization model is given by

$$M(H) = \int_0^\infty \int_{-\infty}^\infty v_1(H_c) v_2(H_i) [\overline{M}(H + H_i; H_c, x)](t) \times dH_i dH_c, \quad (10)$$

where the local average magnetization or kernel \overline{M} quantifies the hysteresis at the lattice level and yields macroscopic models only for homogeneous materials with negligible interaction fields, that is when the effective field $H_e = H + H_i$ is simply the applied field H . In the absence of thermal activation, \overline{M} has the form (employing Preisach notation)

$$[\overline{M}(H; H_c, x)](t) = \begin{cases} [\overline{M}(H; H_c, x)](0) & \text{if } H > H_c \\ \frac{\mu_0}{\eta} H - M_R & \text{if } -H_c < H < H_c \\ \frac{\mu_0}{\eta} H + M_R & \text{if } H < -H_c \end{cases} \quad (11)$$

for the respective cases $\{\tau(t) = \emptyset\}$, $\{\tau(t) \neq \emptyset \text{ and } H(\max \tau(t)) = -H_c\}$, $\{\tau(t) \neq \emptyset \text{ and } H(\max \tau(t)) = H_c\}$. In this expression,

$$H_c = \frac{\eta}{\mu_0} (M_R - M_I) \quad (12)$$

denotes the coercive field and

$$\tau(t) = \{t \in (0, t_f) | H(t) = -H_c \text{ or } H(t) = H_c\} \quad (13)$$

denotes transition points. The initial moment orientation has the form

$$[\overline{M}(H; H_c, x)](0) = \begin{cases} \frac{\mu_0}{\eta} H - M_R & H(0) \leq -H_c \\ x & -H_c < H(0) < H_c \\ \frac{\mu_0}{\eta} H + M_R & H(0) \geq H_c \end{cases} \quad (14)$$

The local magnetization \overline{M} , given by equation (14) versus magnetic field is shown in Figure 5; comparison between macroscopic magnetization results given by (10) and experimental data is shown in Figure 6.

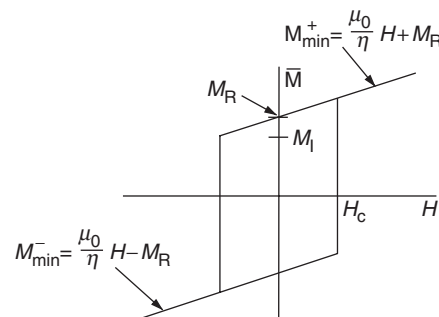


Figure 5. Local magnetization \overline{M} given by expression (14) (Smith et al., 2005).

As detailed in Smith (2005), model equations (10)–(11) can be interpreted as providing an energy basis for certain extended Preisach models, with the kernel \bar{M} derived through thermodynamic considerations providing the Preisach hysterons and the stochastic densities providing the Preisach weights. However, the similarities between the Smith model and the Preisach model are formal rather than conceptual, for several fundamental differences between the two formulations can be established. First, the Smith model, is posed through thermodynamic arguments constructed at the lattice level involving parameters that can be physically correlated with properties of the experimental measurements. Due to its thermodynamic origin, in the Smith model stress and temperature dependencies are incorporated in the kernel rather than the weights as is the case with the Preisach model. The model automatically incorporates these effects without the need for vector-valued weights. This implies that only one set of parameters needs to be identified and no switching between parameter sets is required during real-time operation of the model, thus significantly improving the computational speed relative to the Preisach model.

The strain model for ferromagnetic shape memory materials presented in this article builds on the Smith model for hysteresis of ferroic materials but differs from it in the following aspects. (i) Kernel (8), which characterizes the martensitic volume fraction, was developed by considering the rearrangement of twin variants in martensitic structures and therefore reflects energy functionals which are different from those found in magnetization models. While certain commonality can be established between the proposed model and previous magnetization models – e.g., in regard to double-well energy potentials – the difference between kernels is rooted in the physical differences between

ferromagnetic shape memory and magnetostriction, which were outlined by O’Handley et al. (2000). (ii) In this article, the stochastic homogenization is performed relative to the interaction field H_i and the pinning energy k_2 . This implies that suitable distributions to accommodate these effects can potentially be different than those employed for interaction and coercive fields in Smith et al. (2006). Notwithstanding, for the sake of simplicity, in this article we attempt to exploit certain commonalities between the phenomenological behaviors observed in both models. Namely, for the interaction field we consider a normal distribution centered at $H_i = 0$, as in the Smith model, and for the pinning energy we consider a log-normal distribution similar to that employed in Smith et al. (2006) for coercive fields.

The model thus has the form

$$[x(H, \sigma)](t) = \int_0^\infty \int_{-\infty}^\infty v_1(H_i) v_2(k_2) [\bar{x}(H + H_i; \sigma, k_2)](t) \times dH_i dk_2 \quad (15)$$

where v_1 and v_2 are appropriately chosen distributions and \bar{x} is given by expression (8). Since the Weiss interaction field is known to have both positive and negative values, one possible distribution is

$$v_1(H_i) = c_1 e^{-H_i^2/(2b^2)} \quad (16)$$

which is a normal distribution centered at $H_i = 0$. The pinning energies were incorporated into the energy equations as effective mechanical springs. Thus, the values for k_2 will never be negative. To meet this criterion the distribution over k_2 is chosen to be log-normal,

$$v_2(k_2) = c_2 e^{-(\ln(k_2/\bar{k}_2)/2c)^2}. \quad (17)$$

The effect of this distribution on the slopes of the hysteresis kernels is shown in Figure 7.

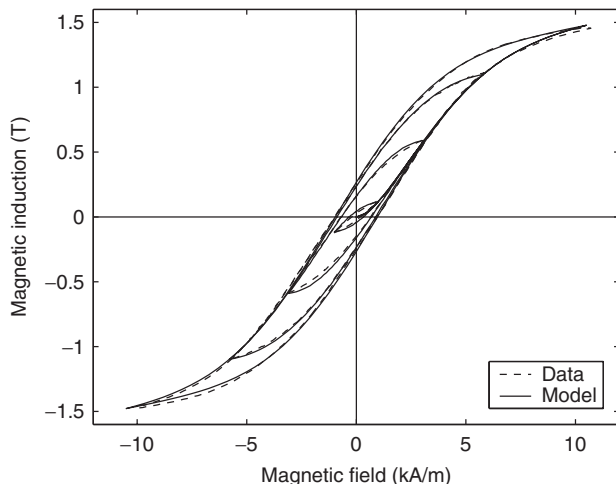


Figure 6. Comparison of steel data with model results obtained from equation (10) (Smith et al., 2005). Copyright © 2005 Society for Industrial and Applied Mathematics. Reprinted with permission.

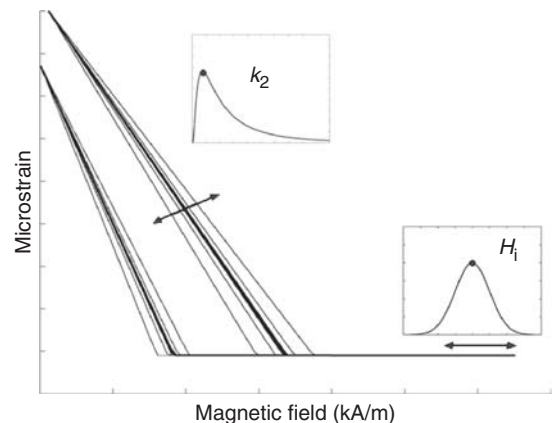


Figure 7. Family of kernels obtained by varying the pinning strength k_2 following a log-normal distribution (inset) and varying the interaction field H_i following a normal distribution (inset).

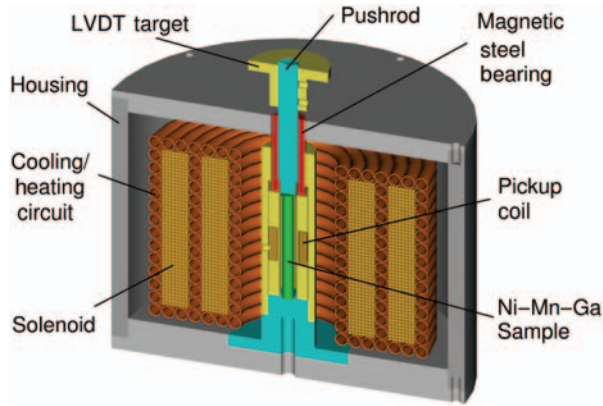


Figure 8. Cross-section of the solenoid transducer employed in this study. Further constructive details are given by Malla et al. (2006).

EXPERIMENTS

A single crystal alloy with composition $\text{Ni}_{50}\text{Mn}_{28.7}\text{Ga}_{21.3}$ was tested for strain response under a [001] sinusoidal magnetic field with an amplitude of 700 kA/m and collinear compressive stresses $\sigma_y = -0.0125, -0.13, -0.27$, and -0.41 MPa. The single crystal ingot, prepared by the Bridgman method at Ames Laboratory, was oriented along the [001] direction and a 0.248 in (0.630 cm) diameter, 0.883 in (2.243 cm) long rod was cut from the ingot using electrical discharge machining (EDM). The experiments were conducted with a collinear magnetic field–stress pair in the solenoid transducer shown in Figure 8, which consists of a water-cooled solenoid, pickup coil, and magnetic steel components integrated to form a closed magnetic circuit. The solenoid consists of 1350 turns of AWG 15 magnet wire and has a field rating of 167 Oe/A. Interspersed within the solenoid lies a 0.25 in-diameter copper coil which provides temperature control within 1°F by means of water flow at a rate of up to 6.35 L/min. The solenoid is driven by two Techron 7790 4 kW amplifiers arranged in series with an overall voltage gain of 60 and a maximum output current of 56 A at a nominal solenoid resistance of $3.7\ \Omega$. The magnetic induction is measured with a pickup coil made from AWG 33 insulated copper wire wound in two layers around an aluminum spool. The strain is measured by a Lucas Shaevitz MHR-025 linear variable differential transducer (LVDT) attached to the pushrod. Several Omega thermocouples are used to monitor the system temperature through a 10-channel Omega signal conditioner. The system is controlled by a DataPhysics data acquisition system interfaced through a PC.

Data collected using this apparatus for compressive loads $\sigma_y = -0.0125, -0.13, -0.27$, and -0.41 MPa are shown in Figure 9, in which the curves have been shifted vertically in such a way that they share a common origin and only the relative deformations are shown

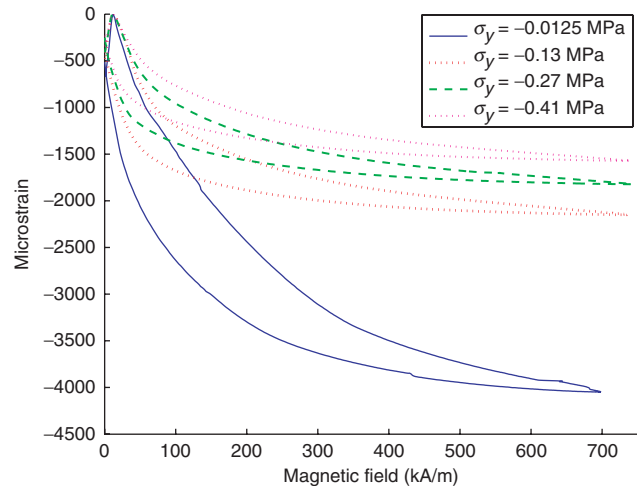


Figure 9. Quasi-static strain vs magnetic field for $\text{Ni}_{50}\text{Mn}_{28.7}\text{Ga}_{21.3}$ at various loads.

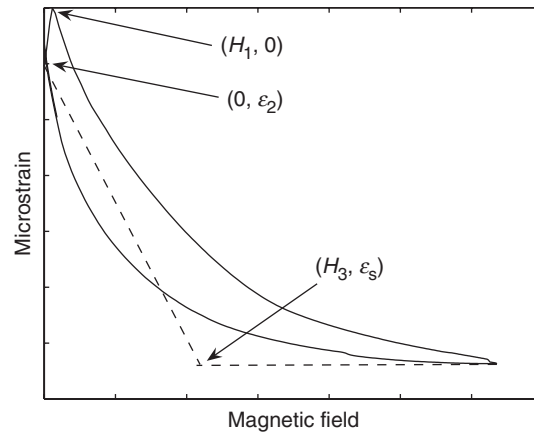


Figure 10. Data points used for identification of model parameters.

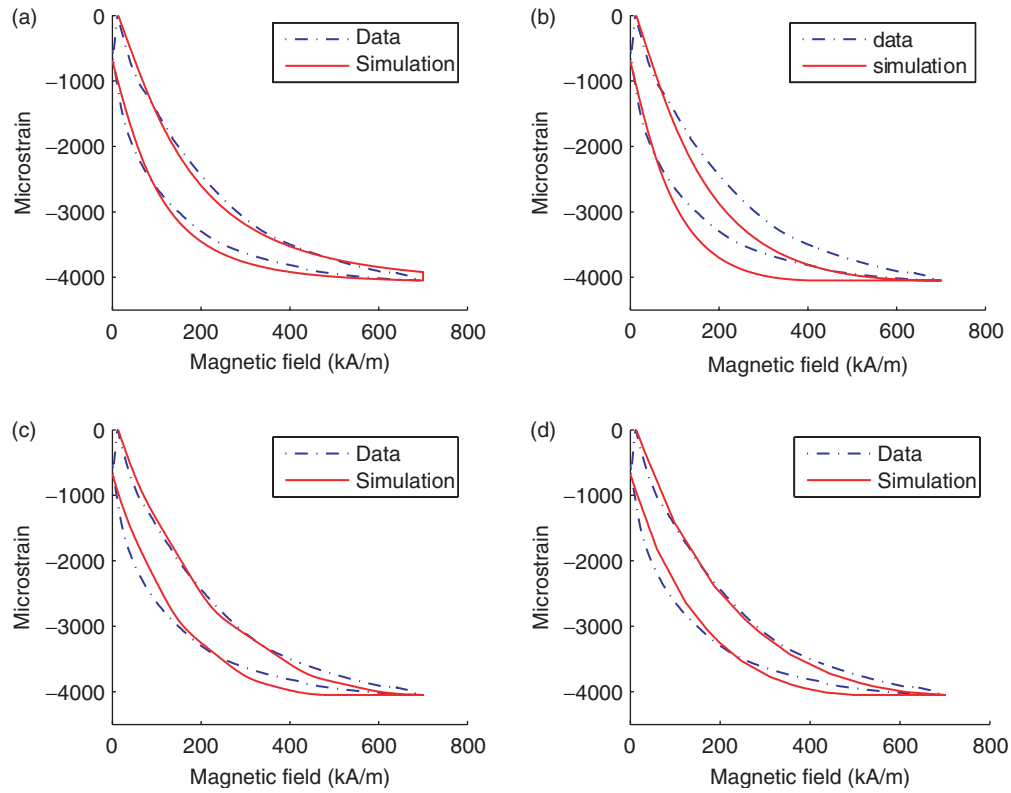
(the unshifted measurements can be found in Malla et al. (2006)). This allows for a direct comparison of model performance for the various relative deformations. Only the half of the butterfly curve corresponding to positive fields is shown; the curves are symmetrical with respect to the abscissa. The maximum strain is -0.41% , which is compressive in agreement with the orientation of the applied field.

MODEL IMPLEMENTATION

The homogenized strain relation (15) was approximated through a composite four-point Gauss–Legendre quadrature routine over 26 intervals in both H_1 and k_2 . Parameters ΔS_{yy} , M_s and Y^{ξ} were obtained from published data (Kiefer and Lagoudas, 2004). As shown in Figure 10, three data points provide the following information: (i) field H_1 at the strain turn around point,

Table 1. Values of model coefficients.

| | |
|--|--|
| Change in mechanical compliance between variants | $\Delta S_{yy} = 0$ |
| Saturation magnetization | $M_s = 622 \text{ kA/m}$ |
| Onset of variant reorientation | $Y^x = 0.2 \times 10^6 \text{ N/m}^2$ |
| Theoretical maximum strain | $\epsilon_{th} = -60000 \times 10^{-6}$ |
| Density | $\rho = 1$ |
| Cell reorientation energy, variant 1 | $c_1 = \epsilon_s(\sigma_y)\sigma_y + \left(\frac{1}{2}\right)\Delta S_{yy}\sigma_y^2 + \mu_0 M_s H_1 - Y^x \text{ J/m}^3$ |
| Cell reorientation energy, variant 2 | $c_2 = \epsilon_s(\sigma_y)\sigma_y + \left(\frac{1}{2}\right)\Delta S_{yy}\sigma_y^2 + Y^x - 2k_2 \frac{\epsilon_2(\sigma_y)}{\epsilon_{th}} \text{ J/m}^3$ |
| First turnaround point | $H_1 = 10,750 \text{ A/m}$ |
| Coercive field distribution | $H_{i,max} = 350 \text{ kA/m}, H_{i,min} = 0$ |
| Pinning energy distribution | $k_{2,max} = 2.7 \times 10^6, k_{2,min} = 2 \times 10^5, \bar{k}_2 = 1.23 \times 10^6$ |
| Standard deviations | $b = c = 1 \times 10^6$ |

**Figure 11.** Comparison of model results and experimental data for the $\sigma_y = -0.0125 \text{ MPa}$ loading condition using various implementation methods: (a) using full distribution; (b) using method (i); (c) using method (ii); and (d) using method (iii).

(ii) strain ϵ_2 at the cross over point, (iii) field H_3 at the onset of saturation, and (iv) saturation strain for each loading case, $\epsilon_s(\sigma_y)$. Values and expressions for the various model parameters are given in Table 1. Coefficients c_1 and c_2 in Equation (8) were determined from experimental data following (Kiefer and Lagoudas, 2004). Distribution parameters \bar{k}_2 , \bar{b} , and c , and kernel parameter n were determined through constrained optimization to minimize the total difference between the time trace strain data and the output of the model for each of the loading conditions.

As an example, a calculated strain versus magnetic field curve is compared to data for the $\sigma = -0.0125 \text{ MPa}$ loading condition in Figure 11(a). The calculated curve shows a non-physical blocky tip due to the inclusion of kernels which fall into non-physical ranges of k_1 and H_i . Figure 12 shows an example of a standard kernel given by relation (8). In the range of parameters where a large k_1 is combined with a large H_i , non-physical kernels with a discontinuity at the maximum field will result. Three methods are considered for addressing this

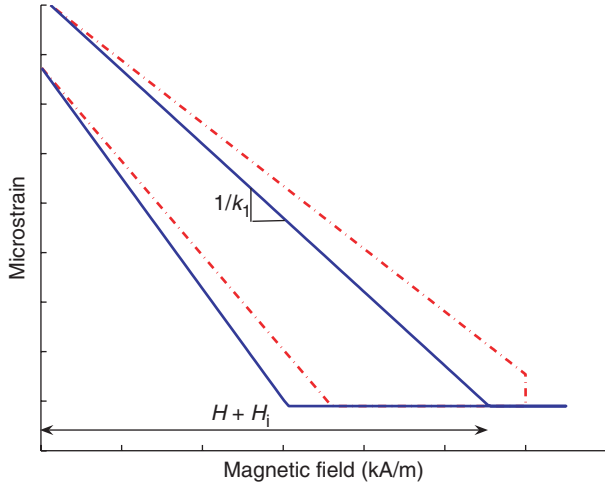


Figure 12. Hysteresis kernels produced by relation (8) showing both physical and non-physical behaviors.

Table 2. Error e associated with each of the methods used to eliminate the discontinuity at maximum field.

| | Original | Method (i) | Method (ii) | Method (iii) $p = 0.1$ |
|---------------------------------------|----------|------------|-------------|---------------------------|
| Σe | 42,382 | 130,000 | 71,818 | 69,960 |
| $\langle e \rangle$ | 52.324 | 160.64 | 88.665 | 86.371 |
| $\langle e \rangle / \epsilon_s (\%)$ | 1.3 | 3.9 | 2.2 | 2.1 |
| $\max(e)$ | 334.15 | 447.56 | 361.75 | 379.94 |

anomalous behavior:

- (i) Discard the kernels that yield non-physical results among the set of kernels found through constrained optimization and the full distributions (16) and (17), and calculate relation (15) based on the reduced set.
- (ii) Truncate the distributions (16) and (17) such that the range of pinning energies and interaction fields that yield non-physical behaviors are discarded, identify new parameters through constrained optimization, and calculate relation (15) based on the truncated distributions.
- (iii) Impose the restriction directly on the bounds employed in the constrained optimization algorithms, such that all the resulting kernels are forced to yield physical results.

The results obtained with these three methods for the $\sigma = -0.0125$ MPa loading condition are shown in Figure 11(b)–(d), while the associated model errors are quantified in Table 2. All three methods yield results without the non-physical discontinuity at maximum field. As expected, the error is greatest for the first method where the non-physical kernels are ignored without recalculating the parameters. The lowest error is

achieved using method (iii), in which the constrained optimization routine includes the inequality

$$\frac{1}{2\rho k_{1,\max}} \left(\epsilon_s \sigma_y + \frac{1}{2} \Delta S_{yy} \sigma_y^2 + \mu_0 M_s (H_{\max} - H_{i,\max}) - \rho c_1 - Y^x \right) \geq p \frac{\epsilon_s}{\epsilon_{th}} \quad (18)$$

which is derived from expression (8) and places limits on the distribution coefficients and therefore the shape of the distributions. Parameter p is introduced to control the percentage of the kernels that are allowed to be non-physical and thus define both the range of allowable distribution shapes and how much of each distribution is truncated. The maximum values for k_1 and H_i are found from expressions (16) and (17),

$$H_{i,\max} = \sqrt{-2(\bar{b})^2 \ln(0.01)} \quad (19)$$

$$k_{1,\max} = n \bar{k}_2 e^{2c \sqrt{-\ln(0.01)}}. \quad (20)$$

Testing shows that $p = 0.1$ achieves a suitable balance between allowable shape of the distributions and the truncation of those distributions which best minimizes the error. An example of the truncated distributions that result from this kernel reduction scheme are shown in Figure 13. Method (iii) with $p = 0.1$ is used in the following section to study the error for all four loading conditions.

RESULTS

Constrained optimization was used to determine the parameters for each of the four loading cases based on the minimization of the total sum of the error between the modeled and measured time traces of the strain. These parameters, shown in Table 3, were found to be within 10% of those necessary to minimize the mean error in all but two cases. A comparison of the data and the model for each of these loading cases is shown in Figure 14 where it is observed that the simulation closely predicts the data in all cases.

The last column in Table 3 represents the set of parameters found by minimization of the sum of the error across all four loading cases. A comparison between the data and the model results generated with these parameters is shown in Figure 15. Even though these simulations are generated from parameters optimized for overall reduction of error, the predictions are remarkably similar to those obtained using parameters optimized for individual cases in Figure 14. This is an indication that there are multiple minima in the four parameter optimization problem and hence various sets of parameters may produce similarly low values of the error. Figure 15 shows that the optimized parameters allow good correlation with data for the lower three load conditions but the model loses

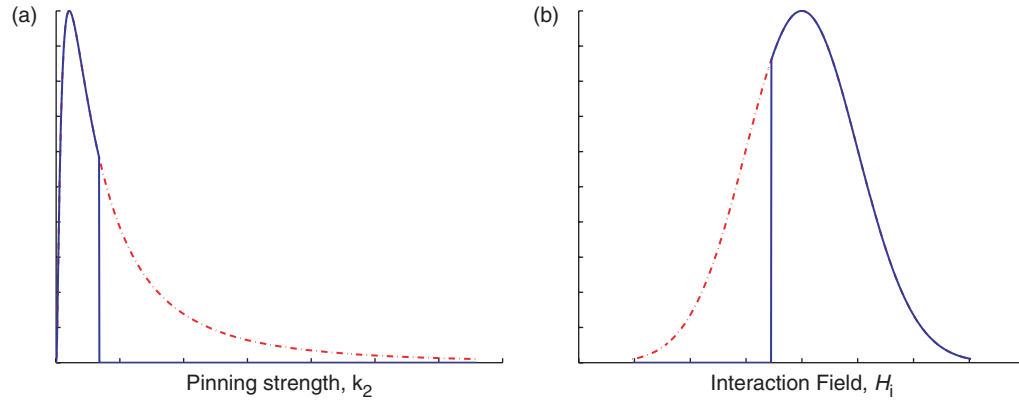


Figure 13. Truncated distributions for (a) pinning strength k_2 and (b) interaction field H_i .

Table 3. Constrained optimization results for parameters under various loads.

| | $\sigma_y = -0.0125$ MPa | $\sigma_y = -20.13$ MPa | $\sigma_y = -0.27$ MPa | $\sigma_y = -0.41$ MPa | Overall optimal |
|-----------|--------------------------|-------------------------|------------------------|------------------------|------------------------|
| n | 1.165 | 1.1417 | 1.0894 | 1.0287 | 1.1207 |
| \bar{k} | 1.0306×10^6 | 0.70091×10^6 | 0.87182×10^6 | 1.3363×10^6 | 0.75325×10^6 |
| c | 0.80761 | 1 | 1 | 0.99856 | 0.99901 |
| \bar{b} | 0.010001×10^4 | 0.012166×10^4 | 0.01×10^4 | 0.01×10^4 | 0.010304×10^4 |

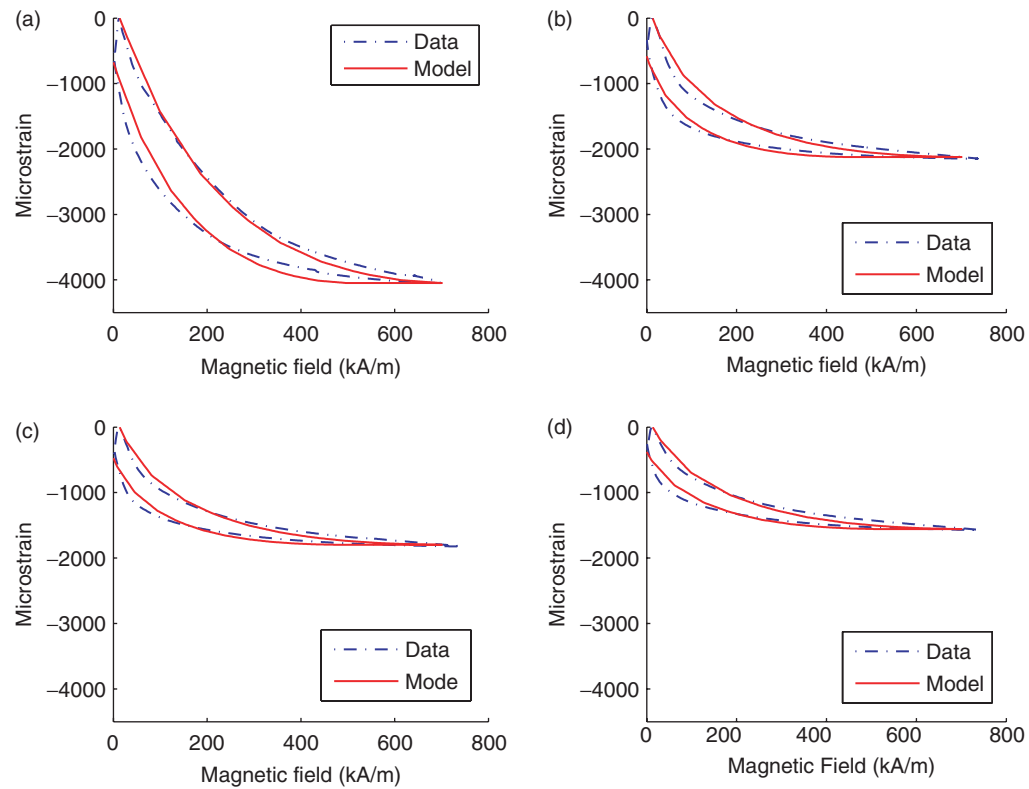


Figure 14. Constrained optimization fits to data for various loads: (a) $\sigma_y = -0.0125$ MPa; (b) $\sigma_y = -0.13$ MPa; (c) $\sigma_y = -0.27$ MPa; and (d) $\sigma_y = -0.41$ MPa.

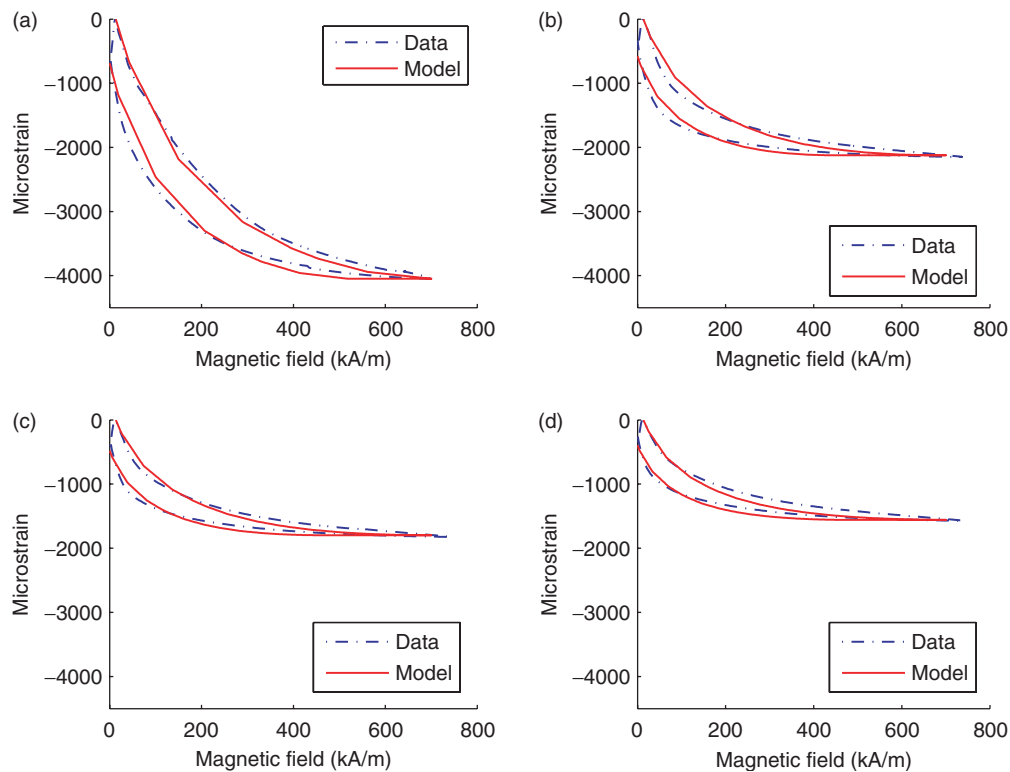


Figure 15. Overall optimized simulation of strain compared to data for various loads: (a) $\sigma_y = -0.0125$ MPa; (b) $\sigma_y = -0.13$ MPa; (c) $\sigma_y = -0.27$ MPa; and (d) $\sigma_y = -0.41$ MPa.

accuracy at the higher load case. This is because the error increase is much steeper for overestimation than for underestimation.

A quantitative look at the error calculations for the constrained optimization for various loading conditions is provided in Table 4. The error measurements calculated include the sum of the error which was the basis for the constrained optimization, the mean of the error, the percent error of the mean with respect to the maximum strain, and the maximum error. The error was calculated as the absolute value of the difference between the data and model at each point. The diagonal of Table 4 indicates the smallest error for all loading values and represents the cases in which the parameters were optimized for the same loading case as that being simulated, which corresponds to the plots shown in Figure 14. The off-diagonal values indicate the error for the cases in which the model parameters were optimized for a load other than the one used in the model. The errors are much larger below the diagonal where parameters for a higher load are used to simulate a lower load than above the diagonal where the reverse is true.

The rightmost column of Table 4 presents the sum of the errors for all four loading conditions for each set of parameters. For all four individually optimized cases the sums of the errors show only an 8% deviation.

The bottom row of the table shows the model error when the set of parameters that minimizes the overall error is used. This total is 12.5% lower than the average sum for the individually optimized cases. In addition, the sum of the error for each loading condition using these overall optimized parameters is within 20% of the minimum sum of the error found for the individually optimized parameters. The maximum is 18% for the $\sigma_y = -0.41$ MPa loading condition which corresponds to the observation made earlier with regard to the decrease in accuracy of the simulations shown in Figure 15 for the higher loading condition. The small differences between the simulations using the four-case optimization parameters and those using the individually optimized parameters highlights the ability of the homogenized model to quantify – from a single set of parameters – the strain produced by Ni–Mn–Ga for various loading conditions.

CONCLUDING REMARKS

Due to exhibiting reduced demagnetization effects and reduced eddy current losses, solenoid transducers can potentially lead to faster and more energy efficient Ni–Mn–Ga devices and systems than their electromagnet counterpart. The design and control of such transducers requires models that are both accurate

Table 4. Error comparison for parameters determined for various loading conditions.

| Parameter set σ_y (MPa) | Loading Case, σ_y (MPa) | | | | Total |
|-------------------------------------|--------------------------------|--------|--------|--------|---------|
| | –0.0125 | –0.13 | –0.27 | –0.41 | |
| –0.0125 | | | | | |
| Σe | 69,960 | 40,393 | 35,767 | 37,644 | 183,764 |
| $\langle e \rangle$ | 86.371 | 49.868 | 44.157 | 46.474 | |
| $\langle e \rangle \epsilon_s (\%)$ | 2.1315 | 2.3049 | 2.4111 | 2.9475 | |
| $\max(e)$ | 379.94 | 320.68 | 222.52 | 164.08 | |
| –0.13 | | | | | |
| Σe | 81,910 | 35,180 | 31,667 | 36,508 | 185,265 |
| $\langle e \rangle$ | 101.12 | 43.432 | 39.095 | 45.072 | |
| $\langle e \rangle \epsilon_s (\%)$ | 2.4957 | 2.0035 | 2.1312 | 2.8564 | |
| $\max(e)$ | 272.85 | 319.42 | 233.88 | 175.12 | |
| –0.27 | | | | | |
| Σe | 81,136 | 39,571 | 29,586 | 31,938 | 182,231 |
| $\langle e \rangle$ | 101.17 | 48.853 | 36.526 | 39.430 | |
| $\langle e \rangle \epsilon_s (\%)$ | 2.4724 | 2.2569 | 1.9908 | 2.4976 | |
| $\max(e)$ | 344.17 | 312.7 | 225.73 | 225.73 | |
| –0.41 | | | | | |
| Σe | 83,168 | 51,065 | 37,442 | 26,615 | 198,290 |
| $\langle e \rangle$ | 102.68 | 63.043 | 46.224 | 32.858 | |
| $\langle e \rangle \epsilon_s (\%)$ | 2.5351 | 2.9196 | 2.5252 | 2.0802 | |
| $\max(e)$ | 455.00 | 406.91 | 251.42 | 189.65 | |
| Optimized | | | | | |
| Σe | 64,106 | 37,297 | 30,965 | 31,454 | 163,822 |
| $\langle e \rangle$ | 79.143 | 46.045 | 38.228 | 38.832 | |
| $\langle e \rangle \epsilon_s (\%)$ | 1.9516 | 2.1255 | 2.0838 | 2.4590 | |
| $\max(e)$ | 324.36 | 317.76 | 231.11 | 171.67 | |

and computationally efficient. With mean errors of under 3%, the proposed modeling technique shows promise as a design and control tool that, in addition, can be used for interpretation of certain physical aspects of Ni–Mn–Ga devices. In particular, the model can provide insight on the interaction between magnetic and elastic properties of Ni–Mn–Ga alloys in cases when the motion of twin boundaries is restrained. The model is constructed on the tenet that pinning sites due to impurities provide the restoring force necessary for bidirectional actuation. While the presence of impurities in Ni–Mn–Ga has been established in the literature, the exact distribution of pinning sites in the alloy investigated is not well understood. For this reason, a phenomenological approach has been utilized based on the identification of Gaussian distribution parameters from experimental data. This method is sufficiently accurate and general for control applications and will motivate the quantification of statistical distributions more closely related to physical properties of the material in future investigations.

ACKNOWLEDGMENTS

The authors thank Ralph Smith and Björn Kiefer for useful discussions, and Thomas Lograsso for supplying

the Ni–Mn–Ga material. The work of L.E.F. is supported by a graduate fellowship from the Ohio Space Grant Consortium. The work of M.J.D. is supported in part by NSF grant #CMS-0409512.

REFERENCES

- Bozorth, R.M. 1951. *Ferromagnetism*, D. Van Nostrand Company, Inc., New York.
- DeSimone, A. and James, R.D. 2002. "A Constrained Theory of Magnetoelasticity," *Journal of the Mechanics and Physics of Solids*, 50:283–320.
- Faidley, L.E., Dapino, M.J., Washington, G.N. and Lograsso, T.A. 2003. "Dynamic Response in the low-kHz Range and Delta-E Effect in Ferromagnetic Shape Memory Ni-Mn-Ga," *Proceedings of ASME IMECE 2003*, #43098, Washington, DC.
- Faidley, L.E., Dapino, M.J., Washington, G.N. and Lograsso, T.A. 2005. "Reversible Strain in Ni-Mn-Ga with Colinear Field and stress," *Proceedings of SPIE Smart Structures and Materials*, Vol. 5761, pp. 501–512, San Diego, California.
- James, R.D. and Wuttig, M. 1998. "Magnetostriction of Martensite," *Philosophical Magazine A*, 77(5):1273–1299.
- Jiles, D.C. 1995. "Introduction to Magnetism and Magnetic Materials," *Magnetism and Magnetic Materials*, Chapman & Hall Publishers, New York, Second edition 1998.
- Kiefer, B. and Lagoudas, D.C. 2004. "Phenomenological Modeling of Ferromagnetic Shape Memory Alloys," *Proceedings of SPIE Smart Structures and Materials*, Vol. 5387, pp. 164–176, San Diego, CA.

- Likhachev, A.A. and Ullakko, K. 2000. "Magnetic-field-controlled Twin Boundaries Motion and Giant Magneto-mechanical Effects in Ni-Mn-Ga Shape Memory Alloy," *Physics Letters A*, 275(1-2):142-151.
- Likhachev, A.A., Sozinov, A. and Ullakko, K. 2001. "Influence of External Stress on the Reversibility of Magnetic-field-controlled Shape Memory Effect in Ni-Mn-Ga," *Proceedings of SPIE Smart Structures and Materials*, vol. 4333, pp. 197-206, San Diego, CA.
- Malla, A., Dapino, M.J., Lograsso, T.A. and Schlager, D.L. 2006. Large Magnetically-induced Strains in $\text{Ni}_{50}\text{Mn}_{28.7}\text{Ga}_{21.3}$ Driven with Collinear Field and Stress," *Journal of Applied Physics*, 99(6): 063903.
- Marioni, M.A., Allen, S.M. and O'Handley, R.C. 2004. "Nonuniform Twin-boundary Motion in Ni-Mn-Ga Single Crystals," *Applied Physics Letters*, 84(20):4071-4073.
- Murray, S.J., Marioni, M., Allen, S.M., O'Handley, R.C. and Lograsso, T.A. 2000. "6% Magnetic-field-induced Strain by Twin-boundary Motion in Ferromagnetic Ni-Mn-Ga," *Applied Physics Letters*, 77(6):886-888.
- Murray, S.J., Marioni, M., Tello, P.G., Allen, S.M. and O'Handley, R.C. 2001. "Giant Magnetic-field-induced Strain in Ni-Mn-Ga Crystals: Experimental Results and Modeling," *Journal of Magnetism and Magnetic Materials*, 226-230 (Part 1):945-947.
- O'Handley, R.C. 1998. "Model for Strain and Magnetization in Magnetic Shape-memory Alloys," *Journal of Applied Physics*, 83(6):3263-3270.
- O'Handley, R.C., Murray, S.J., Marioni, M.A., Nembach, H. and Allen, S.M. 2000. "Phenomenology of Giant Magnetic-field Induced Strain in Ferromagnetic Shape-memory Materials," *Journal of Applied Physics*, 87(9):4712-4717.
- Richard, M.L. 2005. "Systematic Analysis of the Crystal Structure, Chemical Ordering, and Microstructure of Ni-Mn-Ga Ferromagnetic Shape Memory Alloys," PhD Thesis, Massachusetts Institute of Technology, Cambridge, Massachusetts.
- Smith, R.C., Dapino, M.J. and Seelecke, S. 2003. "A Free Energy Model for Hysteresis in Magnetostrictive Transducers," *Journal of Applied Physics*, 93(1):458-466.
- Smith, R.C. 2005. *Smart Material Systems: Model Development*, Society for Industrial and Applied Mathematics, Philadelphia, PA.
- Smith, R.C. and Dapino, M.J. 2005. "A Stress-dependent Hysteresis Model for Ferromagnetic Transducer Materials," *Proceedings ASME IMECE*, #80394, Orlando, FL.
- Smith, R.C., Dapino, M.J., Braun, T.R. and Mortensen, A.P. 2006. "A Homogenized Energy Framework for Ferromagnetic Hysteresis," *IEEE Transactions on Magnetics*, 42(7):1747-1769.
- Sozinov, A., Likhachev, A.A., Lanska, N. and Ullakko, K. 2002. "Giant Magnetic-field-induced Strain in NiMnGa Seven-Layered Martensitic Phase," *Applied Physics Letters*, 80(10):1746-1748.
- Tickle, R. and James, R.D. 1999. "Magnetic and Magnetomechanical properties of Ni_2MnGa ," *Journal of Magnetism and Magnetic Materials*, 195(3):627-638.
- Tickle, R. 2000. "Ferromagnetic shape memory materials," PhD Thesis, Texas A & M, College Station, Texas.
- Wu, G.H., Yu, C.H., Menq, L.Q., Chen, J.L., Yang, F.M., Qi, S.R., Zhan, W.S., Wang, Z., Zheng, Y.F. and Zhao, L.C. 1999. "Giant Magnetic-field-induced Strains in Heusler Alloy NiMnGa with Modified Composition," *Applied Physics Letters* 75(19):2990-2992.